Multilayered Materials Comprising Mesoporous Thin Films and Metal Nanoparticles

Denis Rodríguez-Fernández, Paula C. Angelomé, Galo J. A. A. Soler-Illia, and Luis M. Liz-Marzán*

A novel composite material based on metal nanoparticles (NP) and mesoporous thin films (MPTF), more specifically bilayers of MPTF with a submonolayer of NP deposited between them is introduced. By controlling the deposition conditions, it is possible to build a variety of multilayers including MPTF with different compositions (TiO_2, SiO_2) and pore sizes (templated with cetyltrimethylammonium bromide, F127, Brij 58) and NP of different characteristics and sizes (Au spheres, Au decorated SiO_2). By means of 2D small angle X-ray scattering, transmission electron microscopy, UV–vis spectroscopy, and ellipsometric porosimetry it is demonstrated that NP and MPTF retain their structure and properties within the new material. Importantly, the NP remain accessible for further reactions, a feature that is established by Au overgrowth. Interestingly, the extent of Au growth depends on the mesoporous size and the position of the MPTF with respect to the NP. This new architecture allows the NP to be in direct contact with two different chemical environments and, as a consequence, opens up the possibility to control identity and size of the molecules that can reach them. Thus, the obtained materials may be applied in the development of highly specific sensors and catalysts, in which spatial position plays a fundamental role.

Dr. D. Rodríguez-Fernández, Prof. L. M. Liz-Marzán
Bionanoplasmonics Laboratory
CIC biomaGUNE
Paseo de Miramón 182, 20014 Donostia-San Sebastian, Spain
Dr. P. C. Angelomé
Gerencia Química
Centro Atómico Constituyentes
Comisión Nacional de Energía Atómica
CONICET
Av. Gral. Paz 1499, B1650KNA San Martín, Buenos Aires, Argentina
E-mail: angelome@cnea.gov.ar
Prof. G. J. A. A. Soler-Illia
Instituto de Nanosistemas
Universidad Nacional de General San Martín
CONICET
Av. 25 de Mayo 1021, 1650 San Martín, Buenos Aires, Argentina
Prof. L. M. Liz-Marzán
Ikerbasque
Basque Foundation for Science
48011 Bilbao, Spain

1. Introduction

Composite nanomaterials have been extensively studied in the last years since they present not only the properties of each component but also new features arising from their mutual interaction. Particularly interesting are those nanocomposites based on metal nanoparticles (NP) and mesoporous oxides, which show additional properties derived from the high surface contact between the particles and the film.[1] Metal NP bring to the composite their catalytic and optical properties, which make them one of the most studied nanomaterials in the last decade. The use of NP as catalysts is associated with their high specific surface area and reactivity.[2] On the other hand, the optical properties are related to localized surface plasmon resonances (LSPR)[3] and high electric field enhancements at the NP surface.[4] The optical response of NP depends on their size, shape, and dielectric environment (refractive index of the medium, neighboring NP, etc.) and thus, can be tuned during the synthesis.[5] Due to this close relationship between synthesis, properties, and applications, the preparation of metal NP by colloid chemistry methods has been extensively developed.[6,7]

Ordered mesoporous oxides, on the other hand, bring to the composite their high specific surface area, with a broad range of chemical compositions. This property is directly related to the highly organized array of monodisperse mesopores, whose size can be finely tuned in the 2–10 nm range. This porosity is obtained by using organic molecules as templates, combined with sol–gel reactions that give rise to the oxide walls. By this methodology, a wide variety of mesoporous oxides can be obtained (SiO_2, TiO_2, ZrO_2, mixed oxides, and hybrid oxides), shaped as powders, monoliths, membranes, fibers, and thin films.[8,9] Among all the possibilities, mesoporous oxide thin films (MPTF), prepared using the evaporation induced self-assembly methodology[10] are particularly interesting for the possibility of integration in devices, synthesis flexibility, and their simple manipulation and extraction from reaction media.[11] Additionally, MPTF are ideal to prepare complex tridimensional architectures, using them as building blocks. In that sense, several examples in the literature have demonstrated the possibility of creating bilayers[12–14] and multilayers of MPTF.[15–21]

ADVANCED
SCIENCE NEWS
www.advancedsciencenews.com

Particle
& Particle Systems Characterization
www.particle-journal.com

NP have been combined with MPTF to form nanocomposites.[1] In this case, the NP can be either embedded in the pores,[22–29] within the oxide walls,[30,31] or covered by the MPTF.[32–35] Many of these complex architectures based on MPTF alone or combined with metallic NP have been tested for applications that take advantage of their special properties. In particular, these materials have been used as optical sensors,[17–19,35–37] Surface Enhanced Raman Spectroscopy (SERS) based sensors,[30,33,34,38] catalysts,[26,39–42] photocatalysts,[43–45] photochromic materials,[46–48] and for nonlinear optics.[49,50]

In the present work, a new composite material based on NP and MPTF was designed and built: bilayers of MPTF with NP deposited between them, as a submonolayer. This new architecture allows the NP to be in contact with two different chemical environments in the same region, since they are surrounded by two different MPTF. Both sides of the particles can be accessed through two MPTF with different compositions and pore sizes, which may be used to control the identity and size of the molecules that can reach the particles through the mesopores. As a consequence, the obtained materials may be applied in the development of highly specific sensors and catalysts, in which spatial position plays a fundamental role.

2. Results and Discussion

2.1 Synthesis and Characterization

Nanoparticles and mesoporous oxides thin films were combined, to produce new multilayered architectures in which the spatial position of the components will determine their properties and thus, potential applications. The general scheme followed to produce such composites is illustrated in **Figure 1**.

A first MPTF was deposited by spin coating on top of a glass substrate and stabilized by heating up to 200 °C, without removing the template. Then, the selected NP were deposited on top of the MPTF by means of electrostatic attachment. This step can be performed using polyelectrolytes, but spin coating of a concentrated NP suspension is a simpler and equally efficient alternative for Au NP. Subsequently, the second MPTF was spin coated on top, and the composite material was subjected to thermal stabilization (from 60 to 200 °C). Finally, the micellar templates of both MPTF were extracted by immersion in ethanol. The identity of the two MPTF was varied, in order to
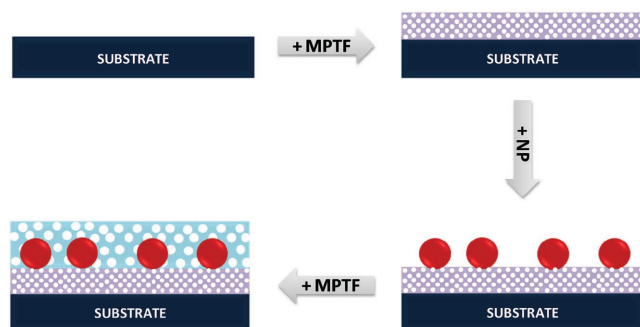

Figure 1. Scheme of the composite preparation: NP are deposited on top of a MPTF and covered by a different MPTF.

Table 1. Description of tested systems. The bottom MPTF is indicated in the rows, the top MPTF in the columns and NP deposited between them are presented in the intersection.

		Top Layer				
		SB	SC	SF	TB	TF
	SB	–	–	Au60	–	Au60
						Au15
						SiO₂ 35
Bottom layer	SC	–	–	Au60	–	Au60
	SF	Au60	Au60	–	Au60	Au15
						SiO₂ 35
	TF	Au60	Au60	–	–	SiO₂ 135

obtain composites with different oxides and pore sizes' combinations. The tested oxides were TiO₂ MPTF templated with Brij 58 and F127 (named TB and TF respectively) and SiO₂ MPTF templated with Brij 58, F127, and cetyltrimethylammonium bromide (CTAB), named SB, SF and SC respectively . On the other hand, NP with different sizes and compositions were encapsulated, to allow the study of its influence on the final properties of the composite materials. Au spheres with 15 and 60 nm diameter (labeled as Au15 and Au60, respectively) and 135 nm diameter SiO₂ spheres decorated with 3 nm diameter Au NP (indicated as SiO₂ 135) were tested. Bilayers were named according to the following code: the first two letters correspond to the inner film (in contact with the substrate), then the code for the NP is included and finally the next two letters correspond to the upper film. Thus, for example, SB/Au60/TF represents a sandwich composed of Brij 58 templated SiO₂ at the bottom and F127 templated TiO₂ in the upper part, with 60 nm Au spheres between them.

In all cases, the films looked smooth and the presence of the NP could be detected by their characteristic colors, by naked eye. All the tested systems are listed in **Table 1**.

To determine the influence of the presence of the particles on the organization of the pores, small angle X-ray scattering with 2D detection (2D-SAXS) experiments were carried out. Shown in **Figure 2** are 2D-SAXS patterns from selected samples, obtained at 4° and 90° incidence.

Figure 2A–D shows the patterns for SB and TF monolayers, respectively. In both cases the patterns demonstrate that a cubic *Im3m* structure was obtained, with the [110] plane oriented parallel to the substrate surface ($a = 8.4$ and 18.6 nm for the SB and TF network, respectively). The full assignment of the cubic structure is presented in Figure S1 (Supporting Information). For the TF case, the structure presents some degree of local order, evidenced by the presence of an ellipse superimposed to the diffraction spots in the pattern obtained at 4°. Also, due to the thermal treatment, the effect of uniaxial contraction in the axis perpendicular to the substrate is observed (ellipsoidal pattern instead of a circular pattern), in agreement with previous results.[51] Figure 2E,F shows the 2D-SAXS pattern for a SBTF bilayer, where two distinct ordered structures are clearly visible, indicating that the characteristics of the monolayers are maintained in the bilayer case, as expected.[12] When 60 nm Au NP are deposited in between SB and TF films, a similar result is obtained (Figure 2G,H), meaning that bilayers preserve the
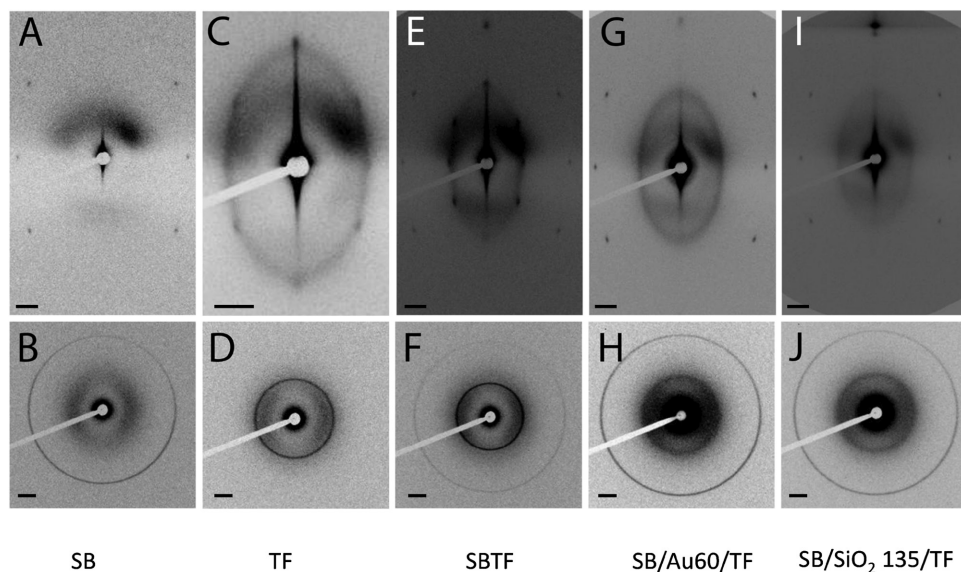
**ADVANCED
SCIENCE NEWS**

www.advancedsciencenews.com

Particle
& Particle Systems Characterization

www.particle-journal.com

Figure 2. A–D) 2D-SAXS patterns of MPTF, E,F) bilayers, and G–J) composite materials containing NP between the MPTF layers, as indicated in the labels. Top row: patterns obtained at 4° incidence. Low row: patterns obtained at 90° incidence. The scale bar represents 10 mm.

order of the corresponding monolayers, with no modification in ordering or interplanar distances due to the presence of the NP between them (see Table S1, Supporting Information). The latter only produce an increase of the scattering intensity at the center of the image. As previously mentioned, different combinations of MPTF and NP were prepared, and they all yielded similar results, i.e., the particle loaded bilayers keep the mesoporous order of the corresponding monolayers, as exemplified for the SBTF system loaded with SiO_2 NP in Figure 2I,J. In all cases, Brij 58 and F127 templated silica or titania films exhibited a cubic *Im3m* structure (in some cases with a certain degree of local ordering), whereas SC films were organized into 3D hexagonal $P6_3/mmc$ structures.

Electron microscopy was also used to characterize the obtained materials. Representative results are presented in **Figure 3**.

Figure 3A,B shows lateral and top view of SF/SiO_2 135/TF sample obtained by scanning electron microscopy (SEM). The top TF film is crack free and fully covers the NP, in which the bright spots corresponding to Au NP that decorate the SiO_2 can be observed. However, from side view, it can be seen that the top film is not smooth, but replicates the NP shape. This behavior is observed only when 135 nm diameter particles are used, whereas smaller NP do not create irregularities on the top film. An example is shown in Figure 3C, for the SC/Au60/TF sample. It can also be seen that the Au particle is fully covered and surrounded by two different environments: TiO_2 with bigger pores (seen on the top film that covers the Au NP, as indicated in the image) and SiO_2 with

smaller pores (that can only be seen in a piece of film detached from the bilayer, as indicated).

UV–vis spectroscopy results (presented in **Figure 4**), are in agreement with those from electron microscopy. In the spectra, it can be seen that the shape of the LSPR band of Au spheres was not altered, indicating that no reshaping or aggregation occurred during the deposition of the particles on top of the mesoporous films (Figure 4A) or the deposition of the second mesoporous layer. The maximum position, however, appears
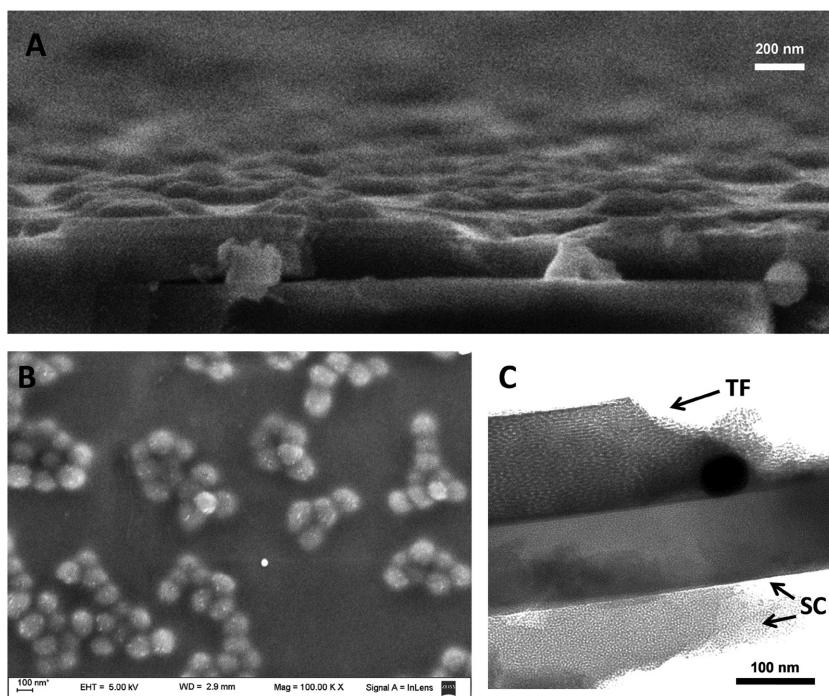

Figure 3. SEM images of the SF/SiO_2 135/TF sample: A) side view and B) top view. C) TEM image of SC/Au60/TF sample.

**ADVANCED
SCIENCE NEWS**

www.advancedsciencenews.com

Particle
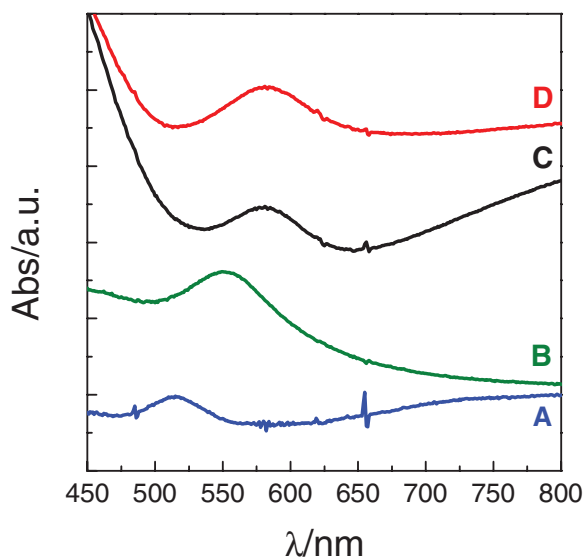& Particle Systems Characterization

www.particle-journal.com

Figure 4. UV–vis spectra of samples: SB/Au60 (A), SB/Au60/SF (B), SB/Au60/TF (C), and SB/Au60/TF after spikes growth (D).

red-shifted due to the refractive index increase around the particles, which varies from $n \approx 1$ (correspondent to particles mostly surrounded by air, maximum position at 514 nm) up to $n = 1.29$ for SF covered particles (Figure 4B, maximum position at 551 nm) or $n = 1.63$ for TF covered particles (Figure 4C, maximum position at 580 nm). These refractive indexes were obtained from environmental ellipsometric porosimetry (EEP) measurements (see below). Finally, the bands observed at higher wavelengths are due to partial light reflection (that results in lower transmission and higher absorbance) caused by the combination of two thin films with different refractive indexes.[15]

Finally, to demonstrate the accessibility of the obtained structure, a complete characterization of the mesoporous thin films bilayers was carried out by EEP. As expected, monolayers displayed similar behavior to that previously reported. However, smaller porosities are obtained, which is due to the use of template extraction instead of calcination. The extraction process involves a lower temperature for the thermal treatment (200 °C instead of 350 °C), which leads to smaller uniaxial contraction of the structure and thus, smaller accesible porosities in all analyzed cases.[52] After characterization of the monolayers, the same analysis was applied to bilayers. The measurements were performed in the bilayers without NP to simplify modeling, but tests were made to demonstrate the accuracy of the obtained results in samples containing NP. Experimentally the process is exactly the same for bilayers, but the modeling is more challenging: each monolayer conforming the bilayer must be modeled separately, using data from the single monolayer as input, so that the most realistic result possible is achieved.[17] Selected results of EEP characterization are presented in **Figure 5** and the analyzed results for the rest of studied systems can be seen in Table S2 in the Supporting Information.

In the top panel of Figure 5, the EEP results for a SB monolayer and the SB layer in the SBTF bilayer, are compared. On the lower panel of Figure 5, the same comparison is made for the TF case. From these plots it can be first observed that
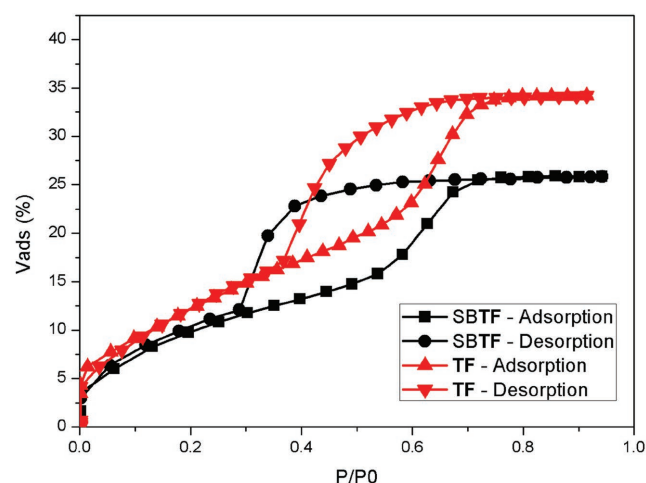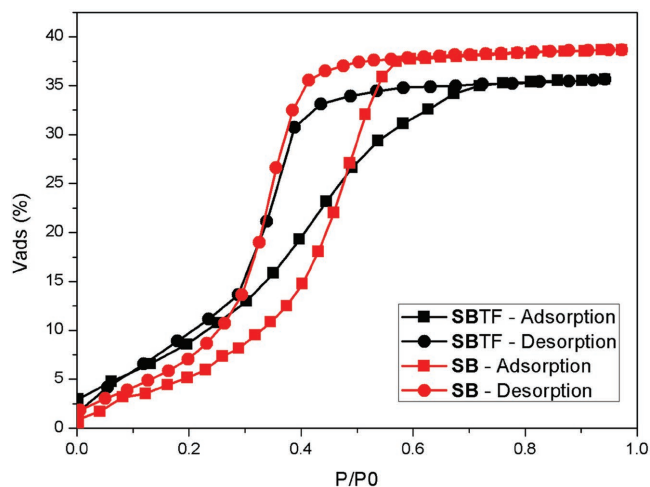

Figure 5. EEP of SBTF sample and the corresponding monolayers. Top panel: SB layer in the bilayer, compared with SB monolayer. Low panel: TF layer in the bilayer, compared with TF monolayer.

both layers remain accessible to water vapor in the bilayer configuration, but porosity decreased for both layers (from 39% to 36% for SB and from 34% to 26% in TF). These results are in close agreement with previously obtained results for calcined bilayers, indicating again the effectiveness of the solvent extraction method to remove the templates. Other synthesized bilayers yielded similar results, demonstrating that in all cases both MPTF are accessible to water vapor and thus, it can be expected that the NP located in the interface are connected with the environment by both MPTF sides.

2.2. Growth of AU Nanoparticles

After confirming the preparation of a substrate with an accessible pore network, gold branches were grown over the metallic spheres. A CTAB-Au mixture was prepared and aged for 30 min at 30 °C ([Au(III)] = 0.5×10^{-3} M, [CTAB] = 0.1 M). Then hydrochloric acid ([HCl] = 1.9×10^{-2} M), silver nitrate ([AgNO$_3$] = 0.12×10^{-3} M), and ascorbic acid ([AA] = 0.8×10^{-3} M) were subsequently added prior to introducing a piece

**ADVANCED
SCIENCE NEWS**

www.advancedsciencenews.com

Particle
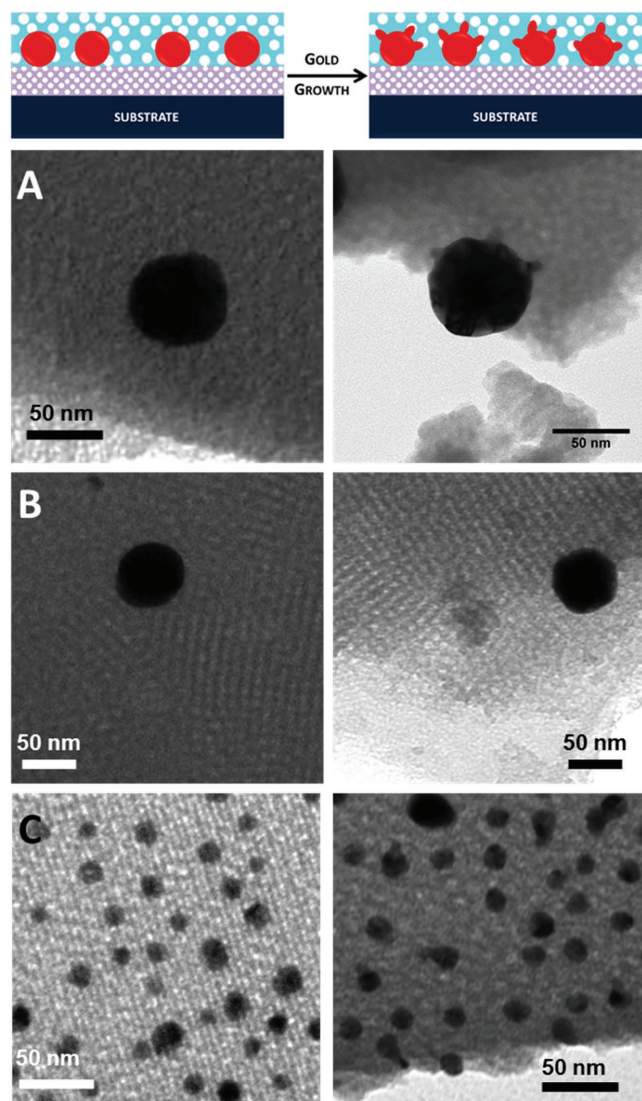& Particle Systems Characterization

www.particle-journal.com

Figure 6. On top: scheme of the gold branches growth for a SB/Au60/TF sample. A–C) TEM images before (left) and after (right) Au NP growth: A) SB/Au60/TF sample, B) TF/Au60/SB sample, and C) SB/Au15/TF sample.

of the mesoporous composite. After 2 h of reaction, the films were removed and washed with ethanol, before characterization. The growth solution became faint pink after the process, indicating some Au NP nucleation that, however, did not affect the growth. Transmission electron microscopy (TEM) images of the obtained materials before and after growth are presented in **Figure 6**, and UV–vis spectra of the SB/Au60/TF sample is presented in Figure 4D.

We expect the branches to grow only through the bigger pores of the F127 templated films, but not in CTAB or Brij 58 templated ones, as was observed previously for NP covered with one layer of MPTF.[32] Also, we expect that the major growth occurs toward the top MPTF layer, since it is the one that covers most of the NP surface (see scheme in Figure 6). TEM images suggest that this asymmetric and preferential growth in fact occurs for the 60 nm Au NP deposited between SBTF

(Figure 6A; Figure S2, Supporting Information) but not for the same particles deposited between and TFSB bilayers (Figure 6B). Moreover, for the SBTF case, the UV–vis spectrum of Au NP after growth (Figure 4D) shows a slight increase in the LSPR band width, compatible with a small extent of tip growth.[32] The obtained information indicates that the growth of NP is spatially defined by the MPTF that surround them. However, since high contrast TEM images can only be obtained for a low amount of isolated NP, more specific characterization is needed to fully confirm the results.

Finally, the possibility of growing 15 nm Au NP was also demonstrated, as can be seen in Figure 6C and Figure S2 (Supporting Information), indicating that the process can be adapted to various Au NP sizes.

3. Conclusions

The possibility of building complex multilayered architectures using MPTF and NP was demonstrated. By controlling the deposition conditions, it was possible to build a wide variety of multilayers including MPTF with different compositions (TiO_2, SiO_2) and pore sizes (templated with CTAB, F127, and Brij 58) and NP of different compositions and sizes (Au spheres, Au decorated SiO_2).

Moreover, the intrinsic characteristics of the different layers are maintained in the multilayered structure. 2D-SAXS measurements confirm that the MPTF show a high degree of organization in the pores and that the presence of the particles does not disturb the order. Also, the NP remain stable when deposited between the films, as demonstrated by electron microscopy and UV–vis spectroscopy. Finally, EEP has shown the high porosity of MPTF layers in the composites, so that the accessibility of the porous structure was high enough to allow species to reach the NP. This feature was demonstrated by Au NP growth: spiked Au particles were obtained, whose growth seems to have directional specificity toward the top layers, if it has F127 templated pores.

The obtained structures may have interesting applications as substrates for surface enhanced Raman scattering[33,34] or in catalysis,[26] using the pore network as a molecular sieve and the metal particles as active material.

4. Experimental Section

Materials: $HAuCl_4\cdot3H_2O$, trisodium citrate dihydrate, $NaBH_4$, HCl (c), tetraethoxysilane (TEOS), Pluronic F127 ($HO(CH_2CH_2O)_{106}(CH_2CH(CH_3)O)_{70}$–$(CH_2CH_2O)_{106}OH$), Brij 58 ($(CH_2CH_2O)_{20}C_{16}H_{33}$), CTAB, poly(diallyldimethylammonium chloride) (PDDA, average molecular weight = 100–200 kg mol^{-1}), poly(sodium 4-styrene-sulfonate) (PSS, average molecular weight = 70 kg mol^{-1}), 3-(aminopropyl)triethoxysilane (APTES), AA, NH_4OH 29%, NaOH, tetrakis(hydroxymethyl) phosphonium chloride (THPC, 80%), and NaCl were supplied by Sigma-Aldrich. Titanium chloride ($TiCl_4$) was supplied by Carlo Erba. Hydrofluoric acid (HF) 40% was purchased from Panreac.

All chemicals were used as received. Pure grade ethanol and Milli-Q grade water were used as solvents.

Particle Preparation: Gold seeds of 15 nm were synthesized by means of the well-known Turkevich method[53] and used without further purification. Using a seeded growth process, these particles were grown

**ADVANCED
SCIENCE NEWS**

www.advancedsciencenews.com

Particle
& Particle Systems Characterization

www.particle-journal.com

up to ≈60 nm, in the presence of CTAB.[54] The resulting spheres were transferred to ethanol using PVP as exchange agent.[55] In order to perform that exchange, 50 mL of CTAB particles was centrifuged at 4000 rpm for 25 min and redispersed in 40 mL of water. Then, 10 mL of the PVP solution (60 molecules nm^{-2}) were added dropwise, stirring the mixture overnight. The modified particles were centrifuged at 4000 rpm for 25 min, and redispersed in 25 mL of ethanol. Finally, the particles were centrifuged under the same conditions and redispersed in 5 mL of supernatant.

Gold seeds of 1–3 nm were prepared according to Duff et al.:[56] NaOH (1.2 mL, 1 M) and aq. THPC (4 mL, 6.8 × 10^{-2} M) were added to H$_2$O (180 mL) under vigorous stirring. After 5 min, aq. HAuCl$_4$ (1.53 mL, 0.13 M) was added in one quick motion. The solution changed instantly from colorless to deep brown.

Silica particles of 135 nm diameter were prepared using a variation of the Stöber method.[57] All glassware was cleaned with an aq. HF solution (2%) before the synthesis. TEOS (0.17 M final concentration) was added to an EtOH solution (250 mL) containing H$_2$O (3.25 M) and NH$_4$OH (0.5 M) under vigorous stirring. When the solution became turbid, stirring was slowed down and continued for 8 h. The silica particles were then washed by four cycles of centrifugation (3400 RCF for 30 min) and redispersion in EtOH. Silica particles were decorated with Au seeds following previously reported procedures.[58,59] First the silica spheres were functionalized with APTES (34 molecules nm^{-2}) in ethanol. Then the particles were washed to remove the excess of silane molecules by 3 cycles of centrifugation (3400 RCF × 30 min) and redispersion in ethanol (0.5 g L^{-1}). Then, using a polyethlylene terephthalate bottle, NaCl (4 mL, 1 M), and silica particles in EtOH (300 µL) were added to freshly prepared gold seeds (40 mL). The mixture was sonicated for 2 min and allowed to reach equilibrium for 12–24 h. The particles were centrifuged (6000 rpm for 30 min) and washed with H$_2$O (3 × 25 mL). Finally, the precursor particles were dispersed in H$_2$O (20 mL) and stored at 4–8 °C.

Preparation of Mesoporous Films: Silica and titania mesoporous thin films were prepared by spin coating onto either glass or another thin film (see below). SiO$_2$ films templated with CTAB, Brij 58 or F127 were spinned at 4000 rpm using 125 µL of solution; whereas titania films templated with Brij 58 or F127 were prepared at 6000 rpm using 50 µL of solution (diluted 2:1 in ethanol and heated up to 40 °C). The detailed composition of film precursor solutions was previously reported.[12] For silica films, solutions comprised of TEOS:EtOH:template:H$_2$O:HCl with a 1:20:0.1:5:0.004 molar ratio for CTAB, 1:40:0.05:10:0.008 for Brij 58, and 1:40:0.005:10:0.008 for F127 were prepared. These solutions were aged for 72 h at room temperature prior to use. For titania films, solutions containing TiCl$_4$:EtOH:template:H$_2$O, with a 1:40:0.05:10 molar ratio for Brij 58, and 1:40:0.005:10 for F127 were employed, with no aging. After spin coating, the films were stored in 50% relative humidity containers (prepared with Ca(NO$_3$)$_2$ saturated solutions in water) for 30 min. Then, the films were thermally treated for 30 min at 60 °C, 30 min at 120 °C, and finally for 2 h at 200 °C. Then the films were covered with particles (see below) and a second mesoporous film was spin coated on top of the first one,[12] following the procedure described above. After deposition, the obtained bilayer was submitted to the same progressive thermal treatment. Finally, the templates of both layers were removed by immersing the films in ethanol for 3 d.

With this synthesis conditions, the obtained film thicknesses were between 60 and 120 nm, depending on the oxide and the template (see Table S2, Supporting Information).

Silica and titania films are labeled as SX and TX, respectively, X being the corresponding template: B represents Brij 58, C corresponds to CTAB, and F to F127. In the case of bilayers, the first two letters correspond to the inner film (in contact with the substrate), and the next two to the upper film. Thus, for example, SBTF represents a sandwich composed of SiO$_2$ and Brij 58 at the bottom and TiO$_2$ and F127 in the upper part, and SB/Au60/TF represents a sandwich composed of SiO$_2$ and Brij 58 at the bottom and TiO$_2$ and F127 in the upper part with 60 nm Au spheres between them.

Attachment of the Particles: For 60 nm Au spheres, 100 µL of particles dispersed in ethanol ([Au] = 2.5 × 10^{-3} M) were spin coated over the films at 6000 rpm for ≈1 s. The process was repeated one more time, with no apparent aggregation (determined by UV–vis spectroscopy).

For 15 nm Au spheres and Au decorated SiO$_2$ NP, a layer by layer approach was used to attach the particles to the MPTF. In the case of Au NP, the first MPTF layer was immersed in a PDDA (1 mg mL^{-1} NaCl 0.5 M) solution for 5 min, rinsed and then immersed in the NP suspension for different times. The maximum loading without aggregation of the NP was achieved after 4 min, as monitored by UV–vis spectroscopy. For the Au decorated SiO$_2$ particles attachment, TX films were immersed for 15 min in a PSS (1 mg mL^{-1} NaCl 0.5 M) solution, then immersed for 15 min in a PDDA (1 mg mL^{-1} NaCl 0.5 M) solution and finally for 60 min in the NP suspension. After each step, the films were thoroughly rinsed with water and dried at air.

It is important to note that higher NP coverages were obtained when layer by layer approach was used, but 60 nm Au spheres could not be properly attached by this methodology, probably due to the presence of CTAB on its surface.

Growth of Gold Branches: A one step method was used, based on the conditions to obtain Au nanorods,[60] to grow spikes on the gold particles deposited between mesoporous films. A small piece of the material was immersed for 2 h in a growth solution of the following concentrations: [Au] = 0.5 × 10^{-3} M, [CTAB] = 0.1 M, [HCl] = 1.9 × 10^{-2} M, [AgNO$_3$] = 0.12 × 10^{-3} M, and [AA] = 0.8 × 10^{-3} M. After the growth step, the films were rinsed with water and dried in air before characterization.

Materials Characterization: A JEOL JEM 1400F transmission electron microscope operating at an acceleration voltage of 120 kV and a Zeiss Supra 40 scanning electron microscope operating at 3.0 kV were used for particle characterization. The TEM grids were first placed over a silicon oxide substrate, then a drop of ethanol was casted over the grid, covering it totally, and then the film was scratched with a blade and put in contact with the ethanol drop. UV–vis spectra were measured with an HP 8453 UV–vis diode-array spectrophotometer. The pore array structure of mesoporous films was analyzed using 2D-SAXS. The measurements were performed at the SAXS2 beamline of Laboratorio Nacional de Luz Sincrotrón (Campinas, Brazil) at 90° and 4° incidence, using λ = 1.55 Å and a MARCCD 2D detector placed at 140 cm of the sample. For these experiments, the samples were deposited onto coverslips to allow the measurements in transmission mode.

The optical properties of SiO$_2$ and TiO$_2$ thin films were measured in ambient conditions (50% RH, 25 °C) using a spectroscopic ellipsometer (SE SOPRA GES5A). From the ellipsometric parameters Δ and Ψ, the film thickness and the refractive index were obtained. Water adsorption–desorption isotherms (at 25 °C) were measured by EEP using the same equipment. The experimental device is based on coupling a pressure controlled chamber and a spectroscopic ellipsometer. The volume of water adsorbed at each P/P_0 (P_0 being the saturation water vapor pressure at 25 °C) is determined by modeling the obtained refractive index according to a three component (water–air–oxide) effective medium approximation, from which the porosity of the film can be estimated. From the adsorption and desorption branches, the pore and neck diameters can be determined using the Kelvin approximation.[61]

Supporting Information

Supporting Information is available from the Wiley Online Library or from the author.

Acknowledgements

[1] P. C. Angelomé, L. M. Liz-Marzán, *J. Sol-Gel Sci. Technol.* **2014**, *70*, 180.

[2] Y. Dai, Y. Wang, B. Liu, Y. Yang, *Small* **2015**, *11*, 268.

[3] M. A. Garcia, *J. Phys. D: Appl. Phys.* **2011**, *44*, 283001.

[4] R. Álvarez-Puebla, L. M. Liz-Marzán, F. J. García de Abajo, *J. Phys. Chem. Lett.* **2010**, *1*, 2428.

[5] L. M. Liz-Marzán, *Langmuir* **2006**, *22*, 32.

[6] Y. Xia, Y. Xiong, B. Lim, S. E. Skrabalak, *Angew. Chem. Int. Ed.* **2009**, *48*, 60.

[7] T. K. Sau, A. L. Rogach, *Adv. Mater.* **2010**, *22*, 1781.

[8] B. Lebeau, A. Galarneau, M. Linden, *Chem. Soc. Rev.* **2013**, *42*, 3661.

[9] D. Gu, F. Schuth, *Chem. Soc. Rev.* **2014**, *43*, 313.

[10] C. J. Brinker, Y. Lu, A. Sellinger, H. Fan, *Adv. Mater.* **1999**, *11*, 579.

[11] P. Innocenzi, L. Malfatti, *Chem. Soc. Rev.* **2013**, *42*, 4198.

[12] P. C. Angelomé, M. C. Fuertes, G. J. A. A. Soler-Illia, *Adv. Mater.* **2006**, *18*, 2397.

[13] M. Faustini, L. Nicole, C. Boissière, P. Innocenzi, C. Sanchez, D. Grosso, *Chem. Mater.* **2010**, *22*, 4406.

[14] T. Brezesinski, M. Antonietti, B. M. Smarsly, *Adv. Mater.* **2007**, *19*, 1074.

[15] M. C. Fuertes, F. J. López-Alcaraz, M. C. Marchi, H. E. Troiani, V. Luca, H. Míguez, G. J. A. A. Soler-Illia, *Adv. Funct. Mater.* **2007**, *17*, 1247.

[16] N. Hidalgo, M. E. Calvo, M. G. Bellino, G. J. A. A. Soler-Illia, H. Míguez, *Adv. Funct. Mater.* **2011**, *21*, 2534.

[17] M. C. Fuertes, S. Colodrero, G. Lozano, A. R. González-Elipe, D. Grosso, C. Boissière, C. Sánchez, G. J. A. A. Soler-Illia, H. Míguez, *J. Phys. Chem. C* **2008**, *112*, 3157.

[18] S. Guldin, M. Kolle, M. Stefik, R. Langford, D. Eder, U. Wiesner, U. Steiner, *Adv. Mater.* **2011**, *23*, 3664.

[19] M. N. Ghazzal, O. Deparis, J. De Coninck, E. M. Gaigneaux, *J. Mater. Chem. C* **2013**, *1*, 6202.

[20] M. N. Ghazzal, O. Deparis, A. Errachid, H. Kebaili, P. Simonis, P. Eloy, J. P. Vigneron, J. De Coninck, E. M. Gaigneaux, *J. Mater. Chem.* **2012**, *22*, 25302.

[21] M. Faustini, D. R. Ceratti, B. Louis, M. Boudot, P.-A. Albouy, C. Boissière, D. Grosso, *ACS Appl. Mater. Interfaces* **2014**, *6*, 17102.

[22] M. C. Fuertes, M. Marchena, M. C. Marchi, A. Wolosiuk, G. J. A. A. Soler-Illia, *Small* **2009**, *5*, 272.

[23] E. D. Martínez, C. Boissière, D. Grosso, C. Sanchez, H. Troiani, G. J. A. A. Soler-Illia, *J. Phys. Chem. C* **2014**, *118*, 13137.

[24] E. D. Martinez, L. Granja, M. G. Bellino, G. J. A. A. Soler-Illia, *Phys. Chem. Chem. Phys.* **2010**, *12*, 14445.

[25] N. Destouches, N. Crespo-Monteiro, G. Vitrant, Y. Lefkir, S. Reynaud, T. Epicier, Y. Liu, F. Vocanson, F. Pigeon, *J. Mater. Chem. C* **2014**, *2*, 6256.

[26] I. L. Violi, A. Zelcer, M. M. Bruno, V. Luca, G. J. A. A. Soler-Illia, *ACS Appl. Mater. Interfaces* **2015**, *7*, 1114.

[27] A. Wolosiuk, N. G. Tognalli, E. D. Martínez, M. Granada, M. C. Fuertes, H. Troiani, S. A. Bilmes, A. Fainstein, G. J. A. A. Soler-Illia, *ACS Appl. Mater. Interfaces* **2014**, *6*, 5263.

[28] A. Calvo, M. C. Fuertes, B. Yameen, F. J. Williams, O. Azzaroni, G. J. A. A. Soler-Illia, *Langmuir* **2010**, *26*, 5559.

[29] M. D. Pérez, E. Otal, S. A. Bilmes, G. J. A. A. Soler-Illia, E. L. Crepaldi, D. Grosso, C. Sanchez, *Langmuir* **2004**, *20*, 6879.

[30] L. Malfatti, P. Falcaro, B. Marmiroli, H. Amenitsch, M. Piccinini, A. Falqui, P. Innocenzi, *Nanoscale* **2011**, *3*, 3760.

[31] L. Malfatti, D. Marongiu, S. Costacurta, P. Falcaro, H. Amenitsch, B. Marmiroli, G. Grenci, M. F. Casula, P. Innocenzi, *Chem. Mater.* **2010**, *22*, 2132.

[32] P. C. Angelomé, I. Pastoriza-Santos, J. Pérez Juste, B. Rodríguez-González, A. Zelcer, G. J. A. A. Soler-Illia, L. M. Liz Marzán, *Nanoscale* **2012**, *4*, 931.

[33] V. López-Puente, S. Abalde-Cela, P. C. Angelomé, R. A. Alvarez-Puebla, L. M. Liz-Marzán, *J. Phys. Chem. Lett.* **2013**, *4*, 2715.

[34] V. López-Puente, P. C. Angelomé, G. J. A. A. Soler-Illia, L. M. Liz-Marzán, *ACS Appl. Mater. Interfaces* **2015**, *7*, 25633.

[35] P. C. Angelomé, L. M. Liz-Marzán, *J. Phys. Chem. C* **2010**, *114*, 18379.

[36] F. Goettmann, A. Moores, C. Boissière, P. Le Floch, C. Sanchez, *Small* **2005**, *1*, 636.

[37] J. Hu, L. Wang, W. Cai, Y. Li, H. Zeng, L. Zhao, P. Liu, *J. Phys. Chem. C* **2009**, *113*, 19039.

[38] Y.-H. Lai, S.-W. Chen, M. Hayashi, Y.-J. Shiu, C.-C. Huang, W.-T. Chuang, C.-J. Su, H.-C. Jeng, J.-W. Chang, Y.-C. Lee, A.-C. Su, C.-Y. Mou, U. S. Jeng, *Adv. Funct. Mater.* **2014**, *24*, 2544.

[39] O. Muraza, E. V. Rebrov, A. Berenguer-Murcia, M. H. J. M. de Croon, J. C. Schouten, *Appl. Catal. A* **2009**, *368*, 87.

[40] L. Ding, W. Li, Q. Sun, Y. He, B. Su, *Chem. - Eur. J.* **2014**, *20*, 12777.

[41] M. Rafti, A. Brunsen, M. C. Fuertes, O. Azzaroni, G. J. A. A. Soler-Illia, *ACS Appl. Mater. Interfaces* **2013**, *5*, 8833.

[42] A. Mitra, D. Jana, G. De, *Chem. Commun.* **2012**, *48*, 3333.

[43] M. Andersson, H. Birkedal, N. R. Franklin, T. Ostomel, S. Boettcher, A. E. C. Palmqvist, G. D. Stucky, *Chem. Mater.* **2005**, *17*, 1409.

[44] I. Bannat, K. Wessels, T. Oekermann, J. Rathousky, D. Bahnemann, M. Wark, *Chem. Mater.* **2009**, *21*, 1645.

[45] J. Zhao, S. Sallard, B. M. Smarsly, S. Gross, M. Bertino, C. Boissiere, H. Chen, J. Shi, *J. Mater. Chem.* **2010**, *20*, 2831.

[46] L. Bois, F. Chassagneux, Y. Battie, F. Bessueille, L. Mollet, S. Parola, N. Destouches, N. Toulhoat, N. Moncoffre, *Langmuir* **2009**, *26*, 1199.

[47] N. Crespo-Monteiro, N. Destouches, L. Bois, F. Chassagneux, S. Reynaud, T. Fournel, *Adv. Mater.* **2010**, *22*, 3166.

[48] L. Nadar, N. Destouches, N. Crespo-Monteiro, R. Sayah, F. Vocanson, S. Reynaud, Y. Lefkir, B. Capoen, *J. Nanopart. Res.* **2013**, *15*, 1.

[49] F. Cui, C. Feng, R. Xie, Z. Hua, X. Cui, J. Zhou, C. Wei, H. Ohtsuka, Y. Sakka, J. Shi, *J. Mater. Chem.* **2010**, *20*, 8399.

[50] Q. Lu, F. Cui, C. Dong, Z. Hua, J. Shi, *Opt. Mater.* **2011**, *33*, 1266.

[51] G. J. A. A. Soler-Illia, P. C. Angelomé, M. C. Fuertes, D. Grosso, C. Boissiere, *Nanoscale* **2012**, *4*, 2549.

[52] I. L. Violi, M. D. Perez, M. C. Fuertes, G. J. A. A. Soler-Illia, *ACS Appl. Mater. Interfaces* **2012**, *4*, 4320.

[53] J. Turkevich, P. C. Stevenson, J. Hillier, *Discuss. Faraday Soc.* **1951**, *11*, 55.

[54] J. Rodríguez-Fernández, J. Pérez-Juste, F. J. García de Abajo, L. M. Liz-Marzán, *Langmuir* **2006**, *22*, 7007.

[55] C. Graf, D. L. J. Vossen, A. Imhof, A. van Blaaderen, *Langmuir* **2003**, *19*, 6693.

[56] D. G. Duff, A. Baiker, P. P. Edwards, *Langmuir* **1993**, *9*, 2301.

[57] G. H. Bogush, M. A. Tracy, C. F. Zukoski, *J. Non-Cryst. Solids* **1988**, *104*, 95.

[58] B. E. Brinson, J. B. Lassiter, C. S. Levin, R. Bardhan, N. Mirin, N. J. Halas, *Langmuir* **2008**, *24*, 14166.

[59] D. Rodríguez-Fernández, J. Pérez-Juste, I. Pastoriza-Santos, L. M. Liz-Marzán, *ChemistryOpen* **2012**, *1*, 90.

[60] L. Scarabelli, A. Sánchez-Iglesias, J. Pérez-Juste, L. M. Liz-Marzán, *J. Phys. Chem. Lett.* **2015**, *6*, 4270.

[61] C. Boissière, D. Grosso, S. Lepoutre, L. Nicole, A. B. Bruneau, C. Sanchez, *Langmuir* **2005**, *21*, 12362.